Journal of Geophysical Research: Solid Earth

Supporting Information for

Influence of Grain-Scale Properties on Localization Patterns and Slip Weakening within Dense Granular Fault gouges

N. Casas [1,2], G. Mollon[1], and A. Daouadji[2]

[1] Univ. Lyon, INSA-Lyon, CNRS UMR5259, LaMCoS, F-69621, France.

[2] Univ. Lyon, INSA-Lyon, GEOMAS, F-69621, France.

Contents of this file

Text S1 to S6
Figures S1 to S6
Tables S1 to S3

Additional Supporting Information (Files uploaded separately)

Captions for Movies S1 to S2

Introduction

This supporting information gives details, methodology and figures that couldn't fit within the paper. It presents a reference table with all the numerical and physical properties of the model (Text S1) and (Table S1). Then biaxial tests are used to characterize the gouge material in the sense of Coulomb-Mohr Theory, they are explained in (Text S2) and (Figure S1). Their detailed results are then gathered in (Table S2) and (Figure S2). (Text S3) and (Figure S3) shows how the shear modulus is computed and its value for each fault gouge sample is presented in (Table S3). (Figure S4) plots the evolution of effective friction as a function of shear modulus. In (Text S4) and (Figure S5), the evolution of the shear modulus is plotted as a function of the number of particles within the gouge thickness. We also show in (Text S5) and (Figure S6), that, for two samples with different geometries, but with the same number of particles within gouge thickness, the obtained results are identical. Finally, the last (Text S6) and (Figure S6), present the effective friction curves for each numerical experiment done with their associated linear weakening slope.

Text S1. Summary of numerical and physical characteristics for the reference sample (MS)

Table S1 gathers all the numerical data settled for the reference matrix sample used in section 3.1 of the paper. Grey values at the top of the table are used for all simulations, whereas the bottom lines are changing depending on the properties tested. The perturbation Pi is not detailed on the paper, it is just used to define the angularity of the polygonal shape of particles.

Table S1. Numerical setup and properties for the numerical campaign (set for reference case). The top part of the table (grey color) concerns properties that do not vary within the simulation campaign.

Property	Associated variable	Value
Normal stress	σ_N	$40\ MPa$
Shear velocity	V	$1\ m/s$
Rock density	ρ_r	2600 kg/m^3
Interparticle cohesion	C_{num}	$500\ MPa$ at boundaries
Interparticle friction	μ_{num}	0.3
Contact stiffness	k_n & k_t	$10^{15}\ Pa/m$
Perturbation	P_i	0.5
Sample size	th_i x Lg	2 x 20 mm
Particle equivalent diameter	ϕ_{eq}	$20\ \mu m$
Number of particles	N	115 825
DEM time step	Δ_t	5.10^{-10} s
Proximity updating period	$\Delta_{t-contact}$	10^{-8}s

Text S2. Characterization of matrix material with biaxial tests

Using a Coulomb-Mohr representation, independent biaxial simulations of samples were run with the characteristics presented for sheared fault gouge (in terms of grain shapes, size distributions, initial solid fraction, interparticle cementation, and interparticle friction). Rectangular granular samples ($4\ mm$ wide and $10\ mm$ high) are placed between four rigid walls. The lower wall is fixed in displacement and the upper wall is submitted to a constant downwards velocity Vy, and the lateral walls are submitted to a confining pressure $\sigma 3$, fixed in vertical and rotational motions, and free to move horizontally. Three tests are performed on the standard case (M-S), with confining stresses of $10\ MPa$, $40\ MPa$, and $80\ MPa$ and for two interparticle stiffnesses ($k_n = 10^{15}, 10^{16}\ Pa/m$), Figure S1 (a) and (b). Vertical stress $\sigma 1$ is monitored during vertical compression, providing a series of pictures of cumulated slip (vertical displacement minus the elastic part), Figure S1 (c). In Figure S1, the slope of shear bands changes between the peak (e) and the plateau (h), this is because the effective friction also changes, corresponding to a reorganization of the failure pattern and a rotation of the stress field. Based on the observed results, Table S2:

- Almost no cohesion is observed for matrix material (in the sense of Coulomb-Mohr), which is in adequation with an incohesive material.

- A change in interparticle stiffness does not have much influence on the internal friction angle but increases the effective friction peak observed, in Table S2. By multiplying by ten the numerical stiffness, the resulting Elasticity modulus is ten times higher. This will probably have an impact on gouge kinematics.
- The orientation angle of the major shear bands formed is growing from the effective friction peak to the steady-state zone, Figure S1 (c).

Figure S2 plots the internal friction angle as a function of the Cohesion (MPa) in the sense of Coulomb-Mohr for standard rocks, for previous results on cemented gouges (Casas et al., 2022) and for the two results from this study.

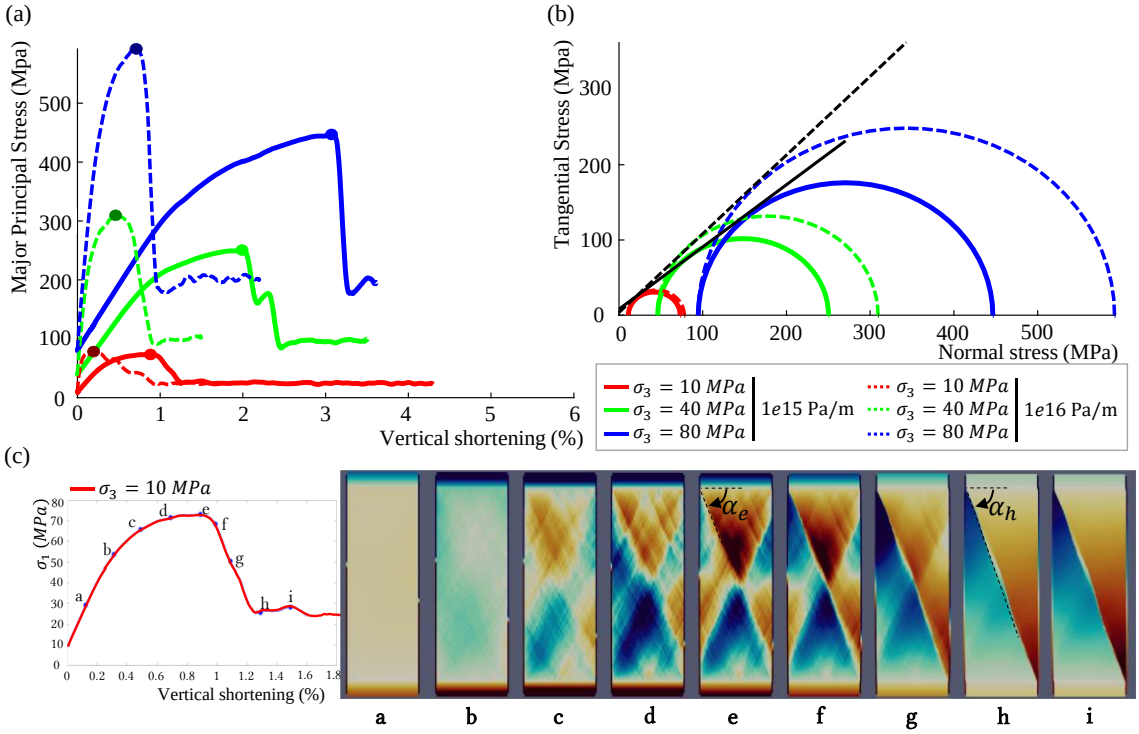

Figure S1. Illustrative results for a standard material (M-S) with different initial interparticle stiffness (a) Major principal stress as a function of vertical shortening, and (b) associated Mohr circles, for three confining stresses (10 MPa, 40 MPa, and 80 MPa) for samples with $k_n = 10^{15}$ Pa/m and $k_n = 10^{16}$ Pa/m. (c) Snapshots of cumulated slip (vertical displacement minus the elastic part) for biaxial experiment with an elastic membrane, for an applied stress $\sigma_n = 10$ MPa for a standard case with $k_n = 10^{15}$ Pa/m. Each point in the curve corresponds to an image above. The evolution of shear bands can be observed and the orientation angle increases with vertical shortening ($\alpha_h > \alpha_e$).

Table S2. Numerical results of the biaxial campaign for two interparticle stiffnesses.

Property	$k_n = 10^{15}$ Pa/m	$k_n = 10^{16}$ Pa/m
Effective friction peak μ_p^*	0.94	1.17
Internal friction angle φ	43.3°	49.5°
Cohesion C	6.4 MPa	2.0 MPa
Elasticity Modulus E	18.96 GPa	118.39 GPa

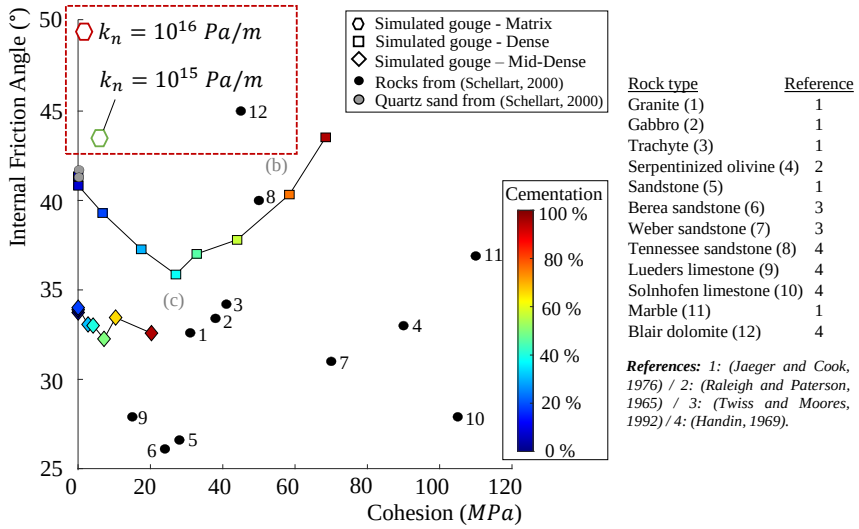

Rock type	Reference
Granite (1)	1
Gabbro (2)	1
Trachyte (3)	1
Serpentinized olivine (4)	2
Sandstone (5)	1
Berea sandstone (6)	3
Weber sandstone (7)	3
Tennessee sandstone (8)	4
Lueders limestone (9)	4
Solnhofen limestone (10)	4
Marble (11)	1
Blair dolomite (12)	4

References: *1: (Jaeger and Cook, 1976) / 2: (Raleigh and Paterson, 1965) / 3: (Twiss and Moores, 1992) / 4: (Handin, 1969).*

Figure S2. Internal friction angle as a function of the cohesion in the sense of Coulomb-Mohr (MPa) for standard rocks, previous cemented gouges studied (Casas et al., 2022), and values obtained for matrix samples with two interparticle stiffnesses.

Text S3. Shear modulus calculi

The shear modulus, Figure S3, can be calculated as

$$G = \frac{\tau}{\gamma_{xy}} = \frac{\tau . th_i}{\Delta_x} \quad (1)$$

where τ is the shearing stress (MPa), th_i the initial gouge width (m) and Δ_x the slip distance at the secant point (m). We compute both the secant shear modulus (at 40% of the maximum shear stress) and the initial tangent shear modulus, Figure S3. The results for all the models are presented in Table S3. The evolution of the effective friction with an increase in shear modulus (respectively with an increase of inter-particle stiffness or size of particles) is presented in Figure S4.

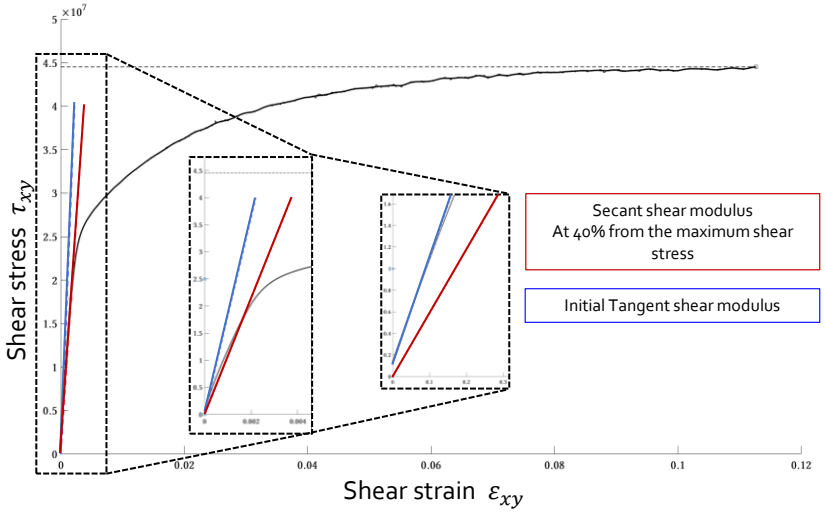

Figure S3. Automatic calculation with Matlab 2020a. Sketch of the shear stress as a function of the shear strain with the secant shear modulus at 40 % of the maximum shear stress (red) and the initial

tangential shear modulus (blue). Example realized for the thin gouge of the standard case (size 20 x 0.2 mm^2, $\mu_{\mathrm{num}} = 0.3$, $\mathrm{k_n} = 10^{15}$ Pa/m, P0.5, $\Phi = 20$ µm).

Table S3. Secant shear modulus and tangential shear modulus for the different gouge samples.

Name	***Size*** $L_g \times th_i$ ***(mm)***	***Friction*** μ_i **-**	***Stiffness*** k_n ***(Pa/m)***	***Diameter*** Φ_i ***(mm)***	***Angular*** P_i **-**	***Gsec*** G_s ***(GPa)***	***Gtan*** G_t ***(GPa)***
M-S	20x2	0.3	10^{15}	0.02	0.5	5.52	10.4
M-S-bis	20x2	0.3	10^{15}	0.02	0.5	5.73	12.2
M-F01	20x2	0.1	10^{15}	0.02	0.5	5.38	12.4
M-F02	20x2	0.2	10^{15}	0.02	0.5	5.71	12.8
M-F06	20x2	0.6	10^{15}	0.02	0.5	5.05	9.04
M-PS-30	20x2	0.3	10^{15}	0.03	0.5	8.36	16.1
M-PS-30-K_{eq}	20x2	0.3	$6.8.10^{14}$	0.03	0.5	6.22	12.2
M-PS-40	20x2	0.3	10^{15}	0.04	0.5	11.2	23.3
M-PS-40- K_{eq}	20x2	0.3	$4.7.10^{14}$	0.04	0.5	6.2	12.2
M-PS-50	20x2	0.3	10^{15}	0.05	0.5	14.1	32.4
M-PS-50- K_{eq}	20x2	0.3	4.10^{14}	0.05	0.5	6.86	13.6
M-Kx2	20x2	0.3	2.10^{15}	0.02	0.5	10.5	24
M-Kx10	20x2	0.3	10^{16}	0.02	0.5	41.9	170
M-P-02	20x2	0.3	10^{15}	0.02	0.2	5.87	9.83
M-P-08	20x2	0.3	10^{15}	0.02	0.8	5.02	10.9
M-Th-1	20x1	0.3	10^{15}	0.02	0.5	5.77	12.2
M-Th-3	20x3	0.3	10^{15}	0.02	0.5	5.41	9.015
M-Th-4	20x4	0.3	10^{15}	0.02	0.5	5.35	9.15

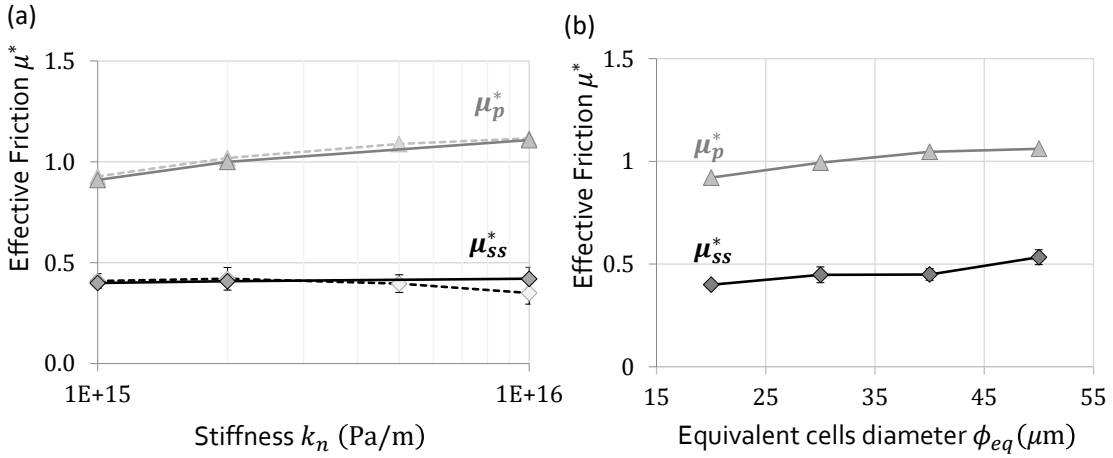

Figure S4. Effective friction as a function of inter-particle stiffness $k_n$at friction peak μ_p^* and steady state μ_{ss}^*. The stiffness increases from respectively $10^{15}\ Pa/m$, $2\ 10^{15}\ Pa/m$, $5\ 10^{15}\ Pa/m$ and $10^{16}\ Pa/m$, for two samples lengths ($L_g = 4\ mm\ and\ 20\ mm$). (b) Effective friction curves for a variation in cells size only (from 20 to 50 µm with an interparticle stiffness of $10^{15}\ Pa/m$).

Text S4. The combined effect of the number of particles within the gouge thickness and shear modulus

Figure S5 presents the Secant shear modulus $G_{sec}\ (GPa)$ as a function of the number of particles within the gouge thickness n_p. A change in gouge thickness and size of particles (with correction of interparticle stiffness) only changes the number of particles within the gouge thickness. Interparticle stiffness changes the shear modulus observed. A change of particles size without a constant value of shear modulus is an artifact and influences both the shear modulus and n_p.

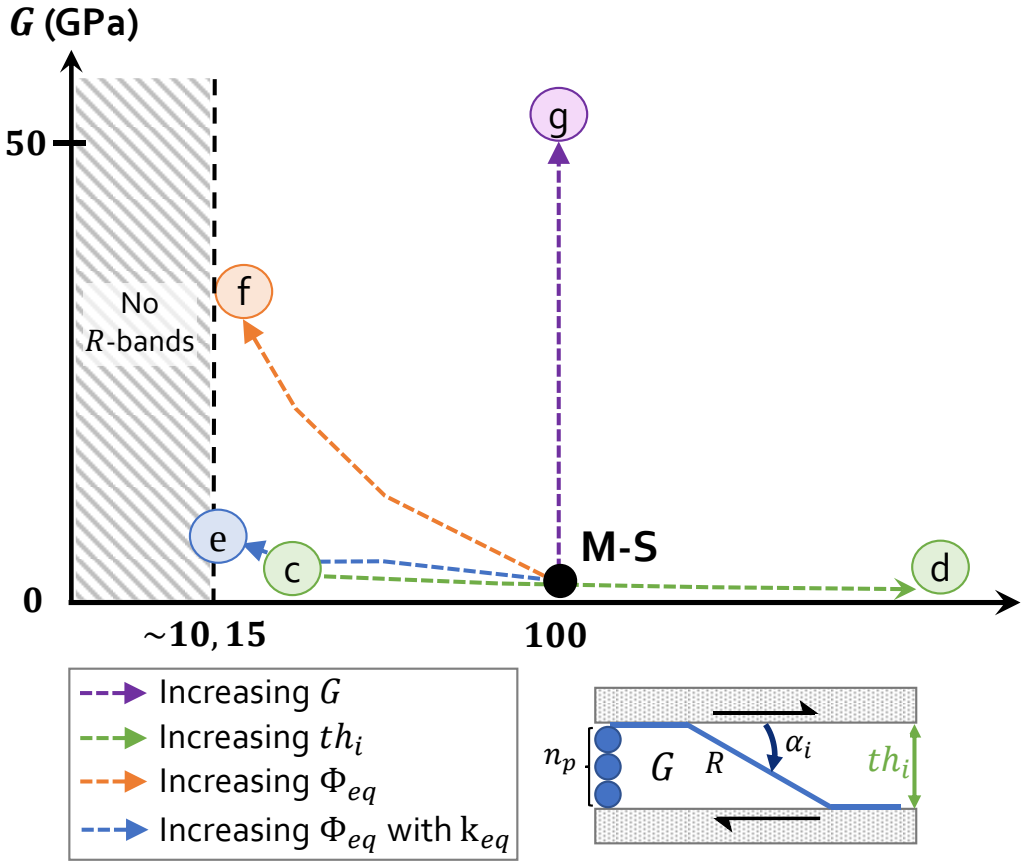

Figure S5. Secant shear modulus $G_{sec}\ (GPa)$ as a function of the number of particles within the gouge thickness n_p. An increase in interparticle stiffness in purple from (M-S) to (g), an increase in the gouge thickness in green from (c) to (d), increase in the size of particles in orange from (M-S) to (f), and increase of the size of particles with corrected equivalent stiffness in blue from (M-S) to (e).

Text S5. Same number of particles within gouge thickness

Figures S6 (a) and (b) present results for two different studies: a change in gouge thickness and a change in the size of particles (with equivalent stiffness). Two gouge samples with a similar number of particles within the gouge thickness ($n_p = 50$) are compared, Figure S6 (c) and (d). They correspond to a sample with an initial thickness of 1 mm and equivalent cells diameter of ϕ_{20} and the sample with an initial thickness of 2 mm and equivalent cells

diameter of ϕ_{40} (with equivalent stiffness of $4.7\ 10^{14}\ Pa/m$). It appeared that the normalized results (friction and dilation) and the deformation within the gouge are identical for the same number of particles within the gouge thickness.

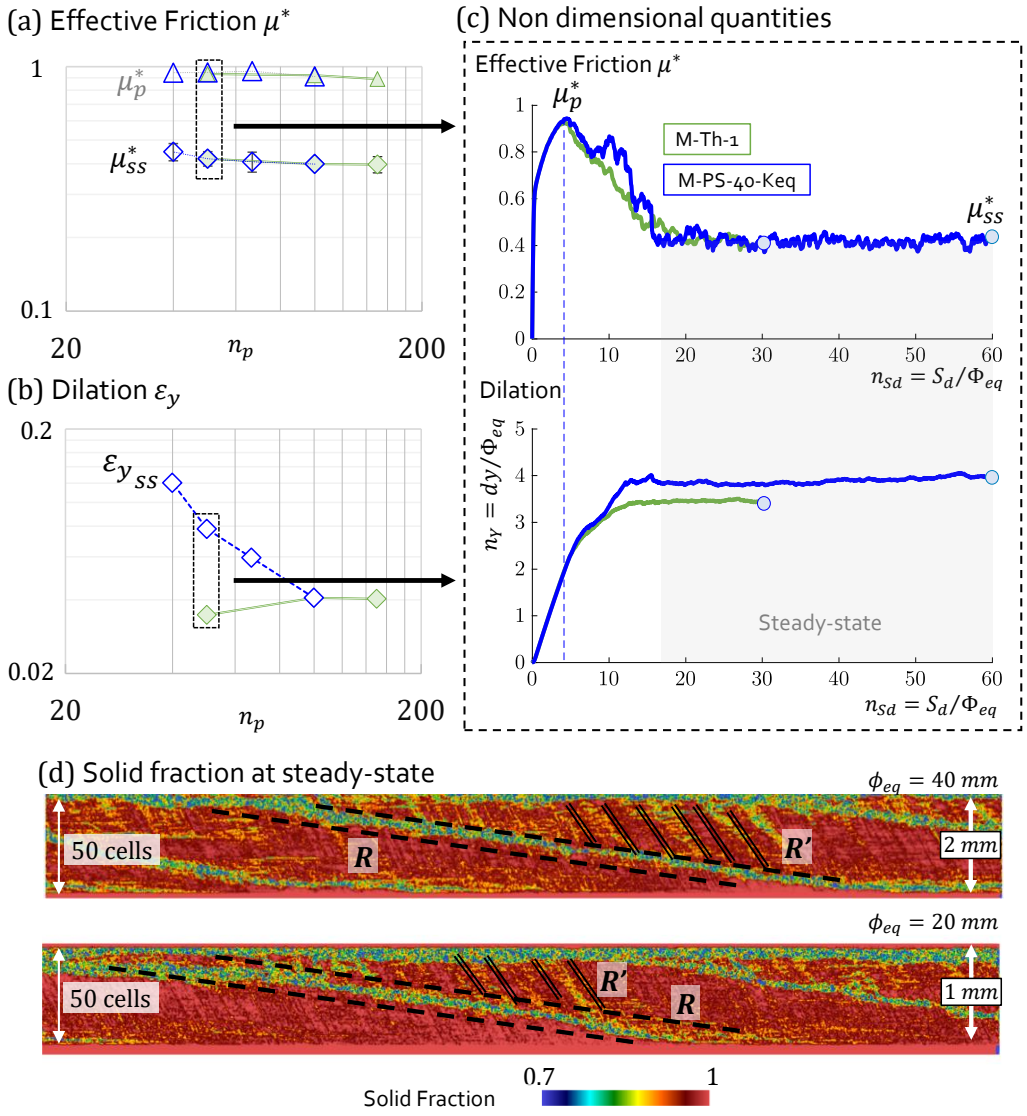

Figure S6. (a) Effective friction as a function of the number of particles within the gouge thickness n_p, (b) averaged dilation at steady-state, obtained for variations in gouge thickness (green) and variations of the size of particles (blue, study with equivalent stiffness). The dashed rectangles surround the two samples with the same number of particles within the gouge thickness ($n_p = 50$ particles) for the sample with an initial thickness of 1 mm and equivalent cells diameter of ϕ_{20} and the sample with an initial thickness of 2 mm and equivalent cells diameter of ϕ_{40} (with an equivalent stiffness of $4.7\ 10^{14}\ Pa/m$**)**. (c) Effective friction μ^* as a function of n_{Sd}, which is the ratio between the fault slip distance S_d and the equivalent diameter of particles ϕ_{eq}. Dimensionless dilation n_Y (number of particles) as a function of n_{Sd}. (d) The solid fraction between 0.7 and 1 at steady-state for the two samples in the hyphen box.

Text S6. Weakening slope

Figure S7 plots the effective friction curves as a function of slip distance for all samples used with the associated linear slope of weakening.

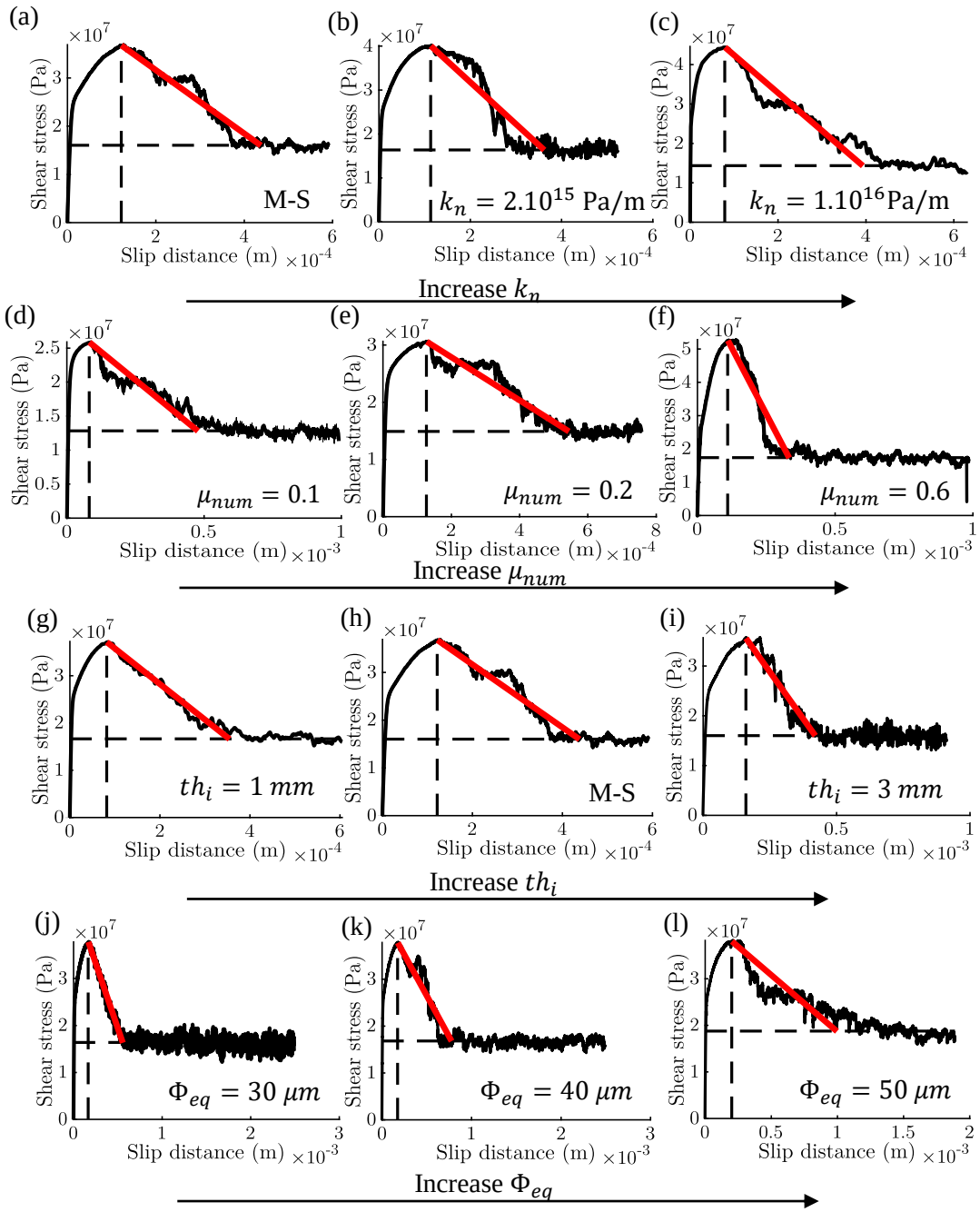

Figure S6. Shear stress (Pa) as a function of the slip distance (m) for matrix models. The red slope is the linear slip weakening slope needed to equal the breakdown energy E_G. (a) to (c) Variation of the interparticle stiffness $k_n = 10^{15} \rightarrow 10^{16}$; (d) to (f) Variation of the interparticle friction $\mu_{num} = 0.1 \rightarrow 0.6$; (g) to (i) Variation of the gouge thickness $th_i = 1 \rightarrow 3$ mm ; (j) to (l) Variation of the size of particles $\Phi_{eq} = 20 \rightarrow 50\ \mu m$ with equivalent stiffnesses.

Movie S1. Riedel localization for the Reference case (MS) for the entire simulation (fast version). The solid fraction is used here to observe the rheology and deformations within the granular gouge. It is the ratio between the total surface of particles on the total surface of gouge (particles and voids). In the present case, it is plotted as a field, i.e. each pixel corresponds to the value of the solid fraction in its close neighborhood. The solid fraction is plotted between 0.8 and 1.

Movie S2. Riedel formation with Kinematics fields for the reference case (MS) for the entire simulation. Normalized x-displacements, y-displacement (m), x-Velocity (m/s) and y-Velocity (m/s)

References

Casas, N., Mollon, G., & Daouadji, A. (2022). DEM Analyses of Cemented Granular Fault Gouges at the Onset of Seismic Sliding: Peak Strength, Development of Shear Zones and Kinematics. *Pure and Applied Geophysics*. https://doi.org/10.1007/s00024-021-02934-5